Measurement 208 (2023) 112476

Contents lists available at ScienceDirect

Measurement

journal homepage: www.elsevier.com/locate/measurement

A design strategy for performance improvement of capacitive sensors for in-flight oil-level monitoring aboard helicopters

Sergio de Gioia [b], Francesco Adamo [a,*], Filippo Attivissimo [a], Daniel Lotano [a], Attilio Di Nisio [a]

[a] Dept. of Electrical and Information Engineering, Polytechnic University of Bari, Via Edoardo Orabona 4, 70125 Bari, Italy
[b] Dept. of Physics "Michelangelo Merlin", University of Bari "Aldo Moro", Via Giovanni Amendola 173, I-70126 Bari, Italy

ARTICLE INFO

Keywords:
Capacitive level sensor
Capillarity
Communicating vessels dynamics
Vibration
Meniscus
Helical capacitor
Avionics

ABSTRACT

Cylindrical capacitors are largely employed in avionic industry as contact submerged probes of level sensors for in-flight oil-level monitoring for many reasons: their high robustness, their long MTBF (Mean Time Between Failures), maintenance-free character, virtually infinite resolution readings and last, relatively low cost. However, the cylindrical capacitors suffer from low sensitivity mainly due to small oil permittivity. This is clearly a disadvantage which collides with the ever-increasing demand for higher static and dynamic performances. To improve that, the approach adopted here consists in tweaking the conventional design of this kind of sensors guided by the study of their limitations in terms of static errors and poor responsiveness caused by phenomena of capillarity, high viscosity, and vibrations. Indeed, sensitivity doubling is proved to be achieved without compromising the indispensable former qualities. This is shown by the results of electrostatic, fluid mechanics, and structural dynamics analyses presented with enough details. Numerical simulations have been carried out and are here presented to confirm results. To summarize, with respect to the conventional capacitive level sensors currently available on the market, the achievements of the proposed design are *i)* an improved sensitivity that, for engine oils, is greater than 700 pF/m, *ii)* a lower cost even though extra-costs for surface perforation must be accounted for, *iii)* cancellation of systematic error due to capillary phenomena and *iv)* improved dynamic response. Also, accurate experimental verifications are being carried out and will be shared in a future paper.

1. Introduction

In avionic industry, the airborne sensor usually employed for oil-level monitoring is a contact cylindrical capacitive sensor made from an air dielectric capacitor with steel plates (referred to as *conventional design* in the sequel). This because it meets the following requirements, all of paramount importance for the avionic industry: *i)* no planned maintenance needs, *ii)* long Mean Time Between Failures (MTBF), *iii)* continuous measurement over the entire dynamic range, *iv)* low cost.

However, additional requirements are increasingly important in terms of both static and dynamic features: *v)* low measurement uncertainty, e.g., less than 1 mm over the entire dynamic range, and *vi)* good dynamic response, with settling times less than 1 s at sudden liquid-level changes of 5% full scale (FS).

These concerns do not seem to be addressed all together in the technical literature, as can be seen from the thorough comparison of capacitive level sensors appeared in [1]. More recently other studies and experimentations have been conducted on capacitive level sensors ([2–6]), but not with reference to the aeronautical context. Specifically, for the avionic industry the most recent works on liquid level measurement pertain to optical sensors [7,8], volume calculation strategies [9] and optic fiber [10,11], but none to capacitive sensors.

This manuscript is aimed at deeply studying a probe for capacitive level sensing on helicopters, starting from the simulated model to validate the final prototype in the near future. Therefore, the conventional design is here revisited with the aim of confirming its longstanding features while at the same time fulfilling the added requirements just said. The approach taken is as follows. Uncertainty reduction is attained with sensitivity increment through inter-plate gap shrinking, compatibly with the availability of standard steel-tube sizes to keep the fabrication

Abbreviations: CLS, Capacitive level sensor.

* Corresponding author.
E-mail addresses: sergio.degioia@poliba.it (S. de Gioia), francesco.adamo@poliba.it (F. Adamo), filippo.attivissimo@poliba.it (F. Attivissimo), d.lotano@phd.poliba.it (D. Lotano), attilio.dinisio@poliba.it (A. Di Nisio).

https://doi.org/10.1016/j.measurement.2023.112476
Received 3 September 2022; Received in revised form 5 January 2023; Accepted 9 January 2023
Available online 12 January 2023
0263-2241/© 2023 Elsevier Ltd. All rights reserved.

costs down. This choice also improves the dynamic response with reduced overshoot and settling time so much as to attain the desired performances, but only within limited dynamic ranges. Unfortunately, the gap reduction also causes capillarity effects to appear, resulting in systematic measurement errors. To limit the capillary rise and further improve dynamic performances, a slit which develops lengthwise all along the lateral surface of the plates is proposed. Since that makes the sensor susceptible to vibrational stresses particularly relevant in helicopters, periodically interspersed interruptions of the slit are then adopted which remedy the stiffness loss that would otherwise ensue.

In what follows the sensor is assumed to have a length of 670 mm and the plates material is assumed to be stainless steel type AISI 316. The engine oil considered is one meeting the standard MIL-PRF-23699G HTS, but what follows applies equally well to other engine oils, like those meeting the standard MIL-PRF-7808.

The scope of this paper is limited to the sensor probe design and analysis and specifically does not encompass the reading electronics. So, the sensitivity and the static and dynamic features here analyzed are to be considered only as component terms of overall quantities for an integrated sensor that would include the said probe. An example of reading electronics is provided in [12].

This work originated in [13] starting from the work in [14]. In section II, the liquid-level measurement uncertainty related to capacitance measurement uncertainty is made explicit for a sensor based on a cylindrical capacitor. An accurate comparison is made between conventional design sensors and narrowed-gap designs allowed by standard sizes of steel tubes. The hydrostatic analysis urged by the hypothesis of narrowing the inter-plate gap is carried out in section III, while in section IV the hydrodynamic analysis is conducted to evaluate the impact of such a narrowing on sensor responsiveness. From the results of these two analyses a lateral slit on the plates is conceived, thus making necessary an electrostatic analysis of a couple of possible slit configurations: straight and helical. This analysis is done in section V, where a capacitance formula of a cylindrical capacitor with open-coil helically wound strip plates is deduced as well. The mathematical derivation details are given in the appendix.

In section VI the proposed sensors are modified to increase their robustness to vibrations commonly found on flying helicopters and their effectiveness is checked with a structural analysis.

Conclusions are highlighted in section VII together with some open points deserving further investigation.

2. Measurement uncertainty and sensitivity

As a guide to find out what design parameters can conveniently be tuned to reduce the measurement uncertainty, the simplest mathematical model is examined which relates the measurand, i.e., the liquid level, to the observed quantity, i.e., the sensor capacitance. A brief explanation about the effects of temperature change of the liquid with respect to the sensitivity is provided. All other influences like liquid composition, contamination with water [15,17], as well as metallic debris [16], are considered constant over time and space.

An air dielectric cylindrical capacitor (not necessarily circular) of capacitance C_0 and length L, when vertically immersed in a tank containing liquid till a certain level h relative to the bottom end of the capacitor may be viewed as the parallel of two cylindrical capacitors with two different dielectrics: *i)* the first is liquid of relative permittivity $\varepsilon_{r,liq}$ with a length equal to the liquid level h, and *ii)* the second is air with a length that is complementary of h to L: $(L-h)$. Hence, the overall capacitance is given by:

$$C(h) = \frac{C_0}{L}\left[h\varepsilon_{r,liq} + (L-h)\right]. \tag{1}$$

Equation (1) is valid provided the liquid is allowed to let in the gap between the plates and assuming that the relative permittivity of air is $\varepsilon_{r,air} = 1$.

This is a linear and thus invertible relationship that permits to evaluate liquid level through the measured capacitance. The sensitivity coefficient $\vartheta h/\vartheta C$ permits the evaluation of the uncertainty of level measurement from the uncertainty of the measured capacitance. However, for design purposes it is better to consider the inverse of this coefficient, that gives the capacitance sensitivity S to liquid level changes:

$$S \overset{\text{def}}{=} \frac{\vartheta C}{\vartheta h} = \frac{C_0}{L}\left(\varepsilon_{r,liq} - 1\right). \tag{2}$$

The *sensitivity* S permits to estimate the admittable uncertainty on capacitance measurements to achieve a given uncertainty on the liquid level measurements. From (2), the sensitivity can be increased only by increasing the capacitance per unit length of the empty sensor C_0/L. Focusing on the circular cylindrical capacitor used in conventional designs:

$$\frac{C_0}{L} = \frac{2\pi\varepsilon_0}{\ln\frac{r_e}{R_i}} = \frac{2\pi\varepsilon_0}{\ln\frac{1}{1-\frac{w}{r_e}}} \tag{3}$$

where r_e is the inner radius of the external plate, R_i is the outer radius of the internal plate and $w = r_e - R_i$ is the gap width. From (3), it is clear that the design parameter to focus on to improve the sensitivity is exactly w/r_e. In particular, this value must be reduced to increase the sensitivity.

In what follows, the geometrical sizes of the plates are chosen among those commonly available according to the European standard EN10220 [18], with the purpose to get higher values of the sensitivity than those of typical conventional sensors. Other international standards can equally well be used. As to the liquid, one with a relative permittivity of 2.15 is considered.

Two designs with narrowed gap are possible, as shown in Table 1, where D_e, t_e, D_i, t_i are the outer diameters and wall thicknesses of the external and internal plates, respectively. The first has almost the same overall size of commercial sensors for avionic applications and the second is the next largest possible. In the following, for the sake of brevity, only the second narrowed-gap design is taken into consideration.

For a similar reason, ε can be considered approximately constant and not influenced by the temperature. In fact, the permittivity changes only by 1.5% when temperature changes from 60 °C to 120 °C [19]. Hence, in the working temperature range of about 100 °C it is possible to consider an average permittivity value, or the dependence on temperature can also be linearized for improved accuracy.

3. Capillary Rise

With such a marked gap-width reduction, capillary effects will appear, and they will cause an additional systematic component in the measurement error. A hydrostatic analysis is mandatory to evaluate the presence and extent of these effects.

The physical problem is that of determining the stable equilibrium state of the free surface of an incompressible liquid in a vertical annular capillary channel (Fig. 1). To determine the capillary rise height, the equilibrium condition to the vertical translation of the liquid column above the bath must be written down.

To that end, only vertical components of the forces acting on such a column need to be considered. In an inertial reference frame, those forces are:

Table 1
Capacitance sensitivity S to liquid-level changes.

D_e[mm]	t_e[mm]	D_i[mm]	t_i[mm]	w[mm]	S[pF/m]	design type
25.4	1,0	19.0	1.0	2.2	307	conventional
21.3	1.2	17.2	1.2	0.85	678	narrowed gap
42.4	3.0	33.7	2.0	1.35	830	narrowed gap

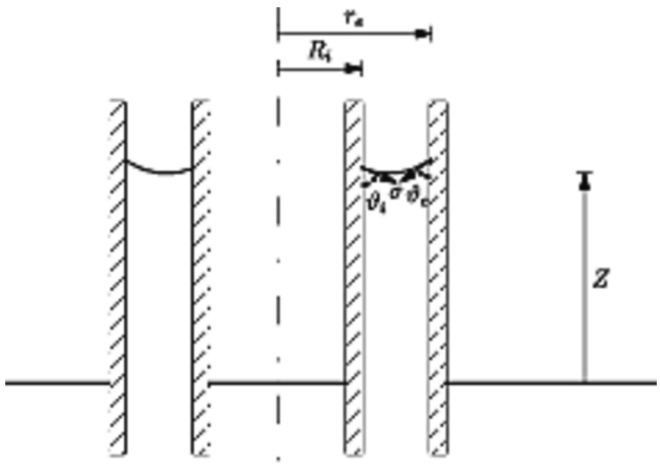

Fig. 1. Longitudinal section of two coaxial pipes immersed in a liquid of surface tension σ and the annular meniscus having contact angles ϑ_i and ϑ_e with the internal and external plates.

- the vertical component of the resultant body force acting in the bulk of the liquid column. They are due to the terrestrial gravitational field[1] and to any vertical acceleration of the tank on which the sensor is installed,
- the vertical component of the resultant capillary force acting on the two circular contact lines between the liquid free surface and the channel walls.

The first one, that is just the liquid column weight if no vertical acceleration is assumed, amounts to $\rho g Z 2\pi\left(r_e^2 - R_i^2\right)$, counted positive downward, where:

- Z is the capillary rise height, that is, the height of the liquid annular column above the bath level,
- ρ is the liquid density,
- g is the gravitational acceleration, then ρg is the liquid specific weight,
- $Z 2\pi\left(r_e^2 - R_i^2\right)$ is the liquid column volume

The second one can be computed by integrating the vertical component of surface tension σ of the liquid–air interface along the contact line made with the internal and external plates. There are two components of constant values $\sigma\cos\vartheta_i$ and $\sigma\cos\vartheta_e$, respectively. ϑ_i and ϑ_e are the contact angles of the liquid free surface with the internal and external plates. The total force is then $2\pi\sigma(R_i\cos\vartheta_i + r_e\cos\vartheta_e)$, counted positive upward.

Equating these component yields the generalized Jurin's law for annular channels, which gives the capillary rise height Z:

$$Z = \frac{2\sigma(R_i\cos\vartheta_i + r_e\cos\vartheta_e)}{\rho g\left(r_e^2 - R_i^2\right)}. \tag{4}$$

The stability and shape of capillary surface in annular channels has been investigated in Seebold *et al.* [20], where the difference between ϑ_i and ϑ_e is shown to vanish with values of R_i/r_e so large as those of the present interest. So, putting $\vartheta_i = \vartheta_e \overset{\text{def}}{=} \vartheta$, (4) simplifies to:

$$Z = \frac{2\sigma\cos\vartheta}{\rho g w}. \tag{5}$$

[1] The effect of the electric field should also be considered; however, for the voltages usually used in these circumstances, it is safely negligible. See also section IV and Equation (7).

From (5), the capillary rise for the narrowed-gap design is 1.6 times greater than that occurring with the conventional design. Assuming $g = 9.81\ \mathrm{m/s^2}$, $\sigma = 30\ \mathrm{mN/m}$ and $\rho = 0.9968\ \mathrm{kg/l}$ at 15°C of the chosen oil Eastman™ Turbo Oil 2197, the maximum value of Z is 4.5 mm in case of perfect wetting corresponding to a zero-contact angle.

4. Transient response

Unfortunately, narrowing the gap prompts for assessing alteration of dynamic behaviour as well, just as it did for the static one. Indeed, the aeronautical application domain mandates fast changes of liquid level to be sensed as early as possible. Hence, a comparison between the transient times of the conventional and of the narrowed-gap designs if mandatory. This can be done by performing a hydrodynamic analysis and simulation. It will result that thanks to a particular nonlinear dynamics markedly influenced by the geometrical sizes, the gap width reduction works in favor of both enhancing settling time in the response to an abrupt level change and eliminating oscillations. This is respectively true for level changes within the first 400 mm and 200 mm of the sensor.

The physical problem is the hydrodynamics of communicating vessels made up of the tank and the inter-plate channel of the sensor joined through its bottom end. It is a special pair of communicating vessels with the cross-section area of one vessel, the tank, enormously greater than that of the other, the annular channel, hence the analysis conducted in [21] is not useful here. Its mathematical solution can be obtained by setting up the dynamic equilibrium among all the pressure components acting on the liquid [22].

Two components are shared between the two vessels: P_{atm} the atmospheric pressure and $\rho g H$ the hydrostatic pressure of the liquid till the bath level H, so neither of them appears in the equilibrium equation. These with the other components are indicated in Fig. 2 together with their positive directions:

- $\rho g Z$ is the hydrostatic pressure due to the liquid column above the bath level, where Z is the capillary rise height.
- P_s is the surface tension pressure.
- P_{ec} is the electrostatic pressure due to any potential difference V applied across the plates.
- ΔP_E is the pressure drop due to local channel entrance losses.
- ΔP_F is the pressure drop due to friction losses in the channel.
- ΔP_a is the acceleration pressure drop.

From section III, P_s is obtained as:

$$P_s = \frac{2\sigma\cos\vartheta}{w}. \tag{6}$$

P_{ec} is due to the fringing field and can be obtained by applying energy balance [23] to give:

$$P_{ec} = \frac{V^2}{2\pi\left(r_e^2 - R_i^2\right)} S. \tag{7}$$

Considering the low voltage values V usually applied during the measurement process, this contribution is safely negligible and will not be considered any longer. Indeed, with the arrangement in [1] the maximum voltage applied is 1.8 V, so $P_{ec} = 9 \bullet 10^{-6}\ \mathrm{N/m^2}$, while hydrostatic pressure of the column above the bath is six orders of magnitude greater. For instance, from (5) at static equilibrium $\rho g Z_{equil} = 44\mathrm{N/m^2}$.

ΔP_E is given by a fraction K of the velocity head:

$$\Delta P_E = K\frac{\rho \dot{Z}^2}{2} \tag{8}$$

where K in case of the entrance to a pipe from a reservoir is usually taken as 0.5 (see for instance [24], p. 300).

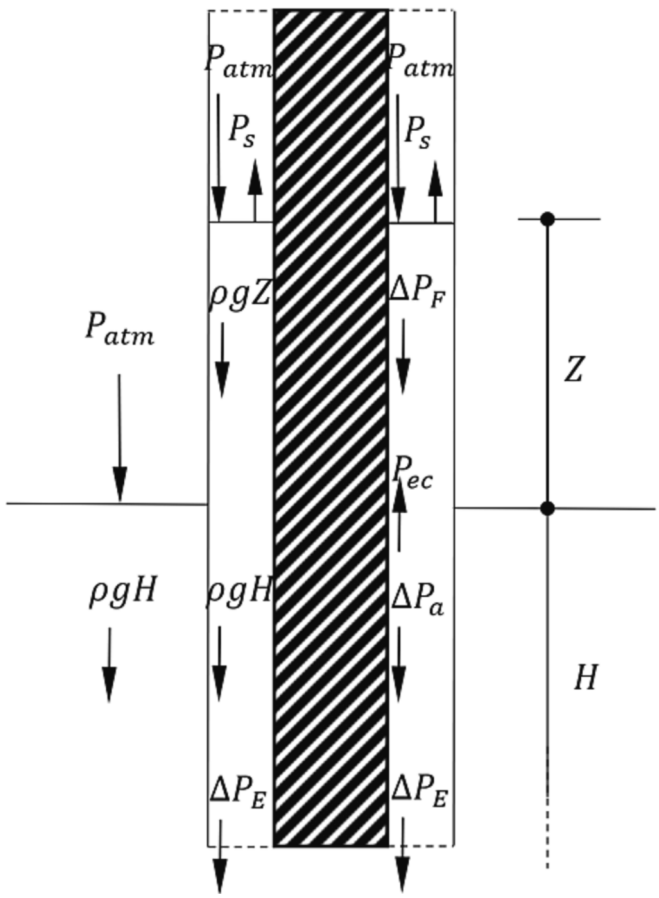

Fig. 2. Longitudinal section of an annular pipe immersed in a tank giving rise to a communicating vessel system with all pression contributions shown together with their positive directions.

In case of laminar flow, ΔP_F can be obtained by applying shell momentum balances ([25], p. 55 or [24], p. 269). For a vertical circular annular channel, the following expression is obtained:

$$\Delta P_F = \frac{8\mu(H+Z)}{\pi r_e^2}\dot{Z}\left[1+\beta^2-\frac{1-\beta^2}{\ln(1/\beta)}\right]^{-1}. \tag{9}$$

Eqn. (9) generalizes to annuli the Hagen-Poiseuille's law for cylindrical pipes by introducing the factor between square brackets. In (9) $\mu = \nu\rho$ is the dynamic viscosity, ν is the kinematic viscosity which for the chosen oil amounts to 5.28 mm^2/s at 100° C and $\beta = R_i/r_e$.

From the Newton's second law, ΔP_a results:

$$\Delta P_a = \rho\ddot{Z}(H+Z). \tag{10}$$

Finally, the dynamic equilibrium is written as:

$$P_s + P_{ec} - \Delta P_E - \Delta P_F - \Delta P_a - \rho g Z = 0 \tag{11}$$

which results in this non-linear ordinary differential equation:

$$\rho\ddot{Z}(H(t)+Z) + K_E\dot{Z}^2 + K_F\dot{Z}(H(t)+Z) + \rho g Z = P_s \tag{12}$$

where K_E and K_F are convenient constants readily derivable from (8) and (9). Through its numerical solution the response to a step liquid-level increase is next shown.

In Fig. 3, six responses to step-up and step-down changes of 5% FS of the tank level for both the conventional and narrowed-gap sensors are shown. Input function and initial condition are such that:

- $H(t) \equiv H(0^+)$ is constant for $t > 0$ with value given by the sum of the initial tank level $H(0^-)$ and of the tank level jump.

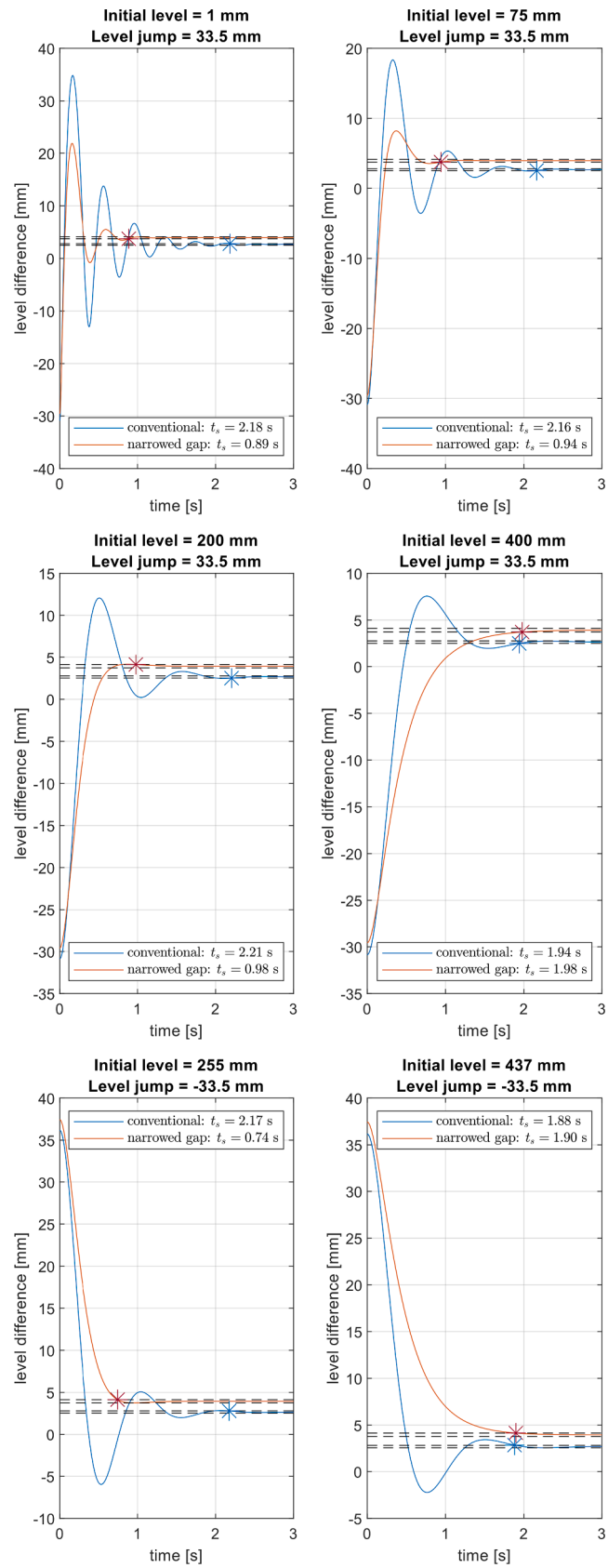

Fig. 3. Temporal evolution of the difference between channel and tank levels Z when abrupt tank-level rise or fall of 5% FS occurs, with indication of settling times t_s (at 5%) for different initial tank levels. A couple of two dashed lines around each steady state value represents the +/-5% band borders. The asterisks mark when the response waveforms settle in the said band.

- $Z(0^+)$ is given by the difference between the meniscus rise $Z(0^-)$ in the channel before the application of the level jump minus the impressed tank level jump.
- $\dot{Z}(0^-) = 0$.

The initial tank levels are chosen purposedly at 1 mm and 75 mm where dynamic behaviour has remarkable features. In these conditions, both designs have an oscillatory response even though less pronounced for the narrowed-gap design which inter alia has shorter settling times. At these initial levels the responses shown are relative to a step-up level change, but the step-down case is analogous.

These characteristics extend up to 200 mm for the step-up response and up to 255 mm for the step-down response. At these levels, the narrowed-gap design ceases its oscillatory behaviour and keeps on outperforming the conventional one in terms of settling times.

At 400 mm for the step-up response and at 437 mm for the step-down response, settling times for the narrowed gap design start to be longer than those of the conventional one which however persists in exhibiting an oscillating response.

From the above results, it can be concluded that narrowing the gap is a good method to substantially improve dynamic performances over the conventional design. The overshoot disappears if the perturbation happens when the liquid level is higher than 255 mm, while the settling time is reduced if the perturbation happens when the liquid level is within 400 mm. Settling time is less than 1 s for levels less than 200 mm as opposed to 2 s of the conventional design.

5. Perforated plate sensors

As seen in section III, narrowing the gap between plates led to a sensible deepening of capillary effect. From this standpoint, it is appropriate to note that if at least one of the walls of the annular channel is cut along its longitudinal length, no column above the bath level can build up in that channel.

The same strategy is useful to dismantle the communicating-vessel configuration between the tank and the annular channel, putting them in direct contact at every height thus avoiding the level equalization sluggishness analyzed in section IV. However, this decreases the sensitivity of the sensor because, as will be shown in detail in the following, the capacitance per unit length reduces. The extent of this reduction depends on the kind of contour along which the cut is made and on its width.

Currently, two configurations for the contour have been taken into consideration: straight and helical. The corresponding sensitivities are determined assuming both plates as perforated along the same kind of contour in such a way that the cuts on the two plates face each other. Specifically, for the helical contours, they can be thought of as formed by intersecting a helicoid with two concentric cylinders representing the plates.

To analytically determine the capacitance of the two configurations, the electric field due to any voltage V applied across the plates is assumed to be present only in those points of the gap belonging to every radial axis that meets both plates. In these points the field is assumed to be radial and dependent only on the radial position of the point. Elsewhere, that is out of the gap and even in the gap between the contours of the removed plate surface, the field is assumed to be null.

This is thus a one-dimensional problem which is easily solved through the Gauss law choosing as the integration surface $S(r)$ a cylinder coaxial with the plates with length L and arbitrarily fixed radius r such that $r_e < r < R_i$. Indeed, the bases of that cylinder account for no contribution to the flux, being the field tangential to them. On the lateral side the field is either null or orthogonal to it and constant with constant value $E_c(r)$, the only unknown of the problem. $E_c(r)$ depends on the contour c). Thereby, the flux is simply $E_c(r)$ times the area $A_c(r)$ of that part of the lateral side of the integration surface where the field is not null but also depending on the contour c. Then:

$$E_c(r) = \frac{Q_c}{\varepsilon_0 A_c(r)} \tag{13}$$

where Q_c is the charge on the internal plate.

The capacitance per unit length is then obtained once the voltage V across the plates, that is the line integral of the field $\vec{E}_c(r)$ along a curve with endpoints on the two plates, is known. Using a radial straight line as the integration line the contour-dependent capacitance C_c per unit length is immediately obtained as:

$$\frac{C_c}{L} = \frac{Q_c}{VL} = \frac{\varepsilon_0}{\int_{R_i}^{r_e} \frac{dr}{b_c(r)}} \tag{14}$$

where $b_c(r) = A_c(r)/L$ is the length of boundary of the cross section of $S(r)$ where the field is not null, that is the circumference of the cross section of $S(r)$ minus the length of boundary of the cross section of $S(r)$ where the field is null.

For the straight-slit case (putting $c = s$ for straight) its value is:

$$b_s(r) = 2\pi r - c_w r \tag{15}$$

where c_w is the angular contour width, that is, the angle under which the aperture of the facing contours is seen from the cylinder axis in any plane perpendicular to the contour itself. For the helical-slit case, putting $c = h$ for helix, it is:

$$b_h(r) = 2\pi r - \frac{c_w r}{sin\gamma(r)} \tag{16}$$

where $\gamma(r)$ is the lead angle of the helical contour, which is such that.

$$sin\gamma(r) = \frac{p}{\sqrt{(2\pi r)^2 + p^2}} \tag{17}$$

where p is the helical pitch.

Solving the integral in (14) and putting $n_w = c_w/2\pi$, the specific capacitance for the sensor with a straight slit is given by.

$$\frac{C_s}{L} = \frac{(1 - n_w)2\pi\epsilon_0}{ln\frac{r_e}{R_i}}. \tag{18}$$

It is less than that of the plain cylindrical capacitor (3) for any positive value of n_w and approaches it as n_w approaches zero. A significantly more complicated expression is expected for the capacitance of the sensor with helical slit. Putting.

$$u(r) = \sqrt{1 + (2\pi r/p)^2} \tag{19}$$

and $u_e = u(r_e)$, $u_i = u(R_i)$, the specific capacitance is now.

$$\frac{C_h}{L} = \frac{2\pi\epsilon_0}{ln\left[\frac{r_e}{R_i}\sqrt{\left|\frac{1-u_e}{1-u_i}\right|^{\frac{n_w}{1-n_w}}\left|\frac{1+u_i}{1+u_e}\right|^{\frac{n_w}{1+n_w}}} \times \left|\frac{1-n_w u_i}{1-n_w u_e}\right|^{\frac{1}{1-n_w^2}}\right]} \tag{20}$$

(see section VIII for details), which is less than that of the straight-slit case, but approaches it as p approaches to infinity, when the helix becomes a straight line as derived in (39)-(40). On the other hand, C_h/L approaches that of the plain cylindrical sensor as n_w approaches zero. In Fig. 4 (18) and (20) are reported as functions of n_w, while in Fig. 5 a family of (20) parametrized by n_w is shown as a function of p/L.

Choosing the following values for the contour parameters.

- $n_w = 1.74 \bullet 10^{-2}$turns, corresponding to a slit width on the internal plate of $2\pi n_w R_i = 1.85$mm
- p = 26.4 mm, shown with highlighted dots in Fig. 4 and Fig. 5
- and as cylinder geometrical parameters those of the former narrowed-gap sensor

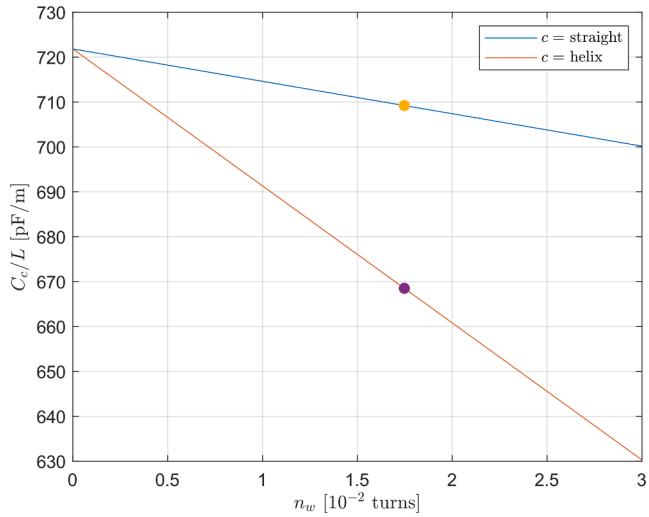

Fig. 4. Air specific capacitance of narrowed-gap CLS with continuous straight and helical slits vs slit aperture width. Highlighted points are those corresponding to the chosen aperture width.

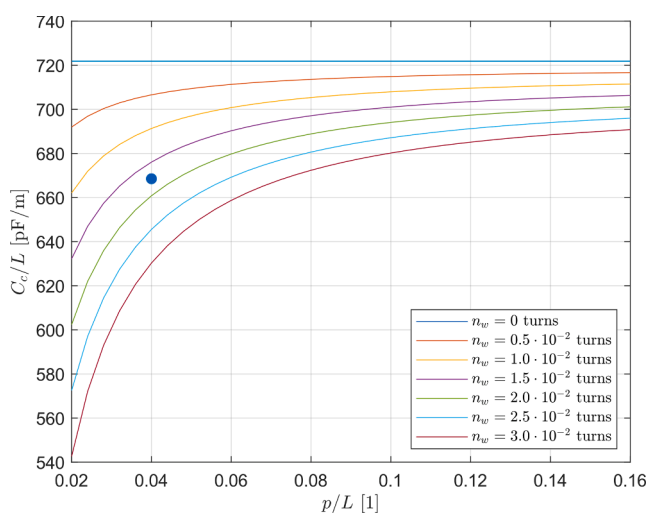

Fig. 5. Air specific capacitance of the helical narrowed-gap CLS for different slit widths vs helix-pitch-to-length ratio. The highlighted point is that corresponding to the chosen slit aperture width and helical pitch.

only a small reduction of the sensitivity results. This reduction is clearly due to the perforation which does not erode the sensitivity doubling gained by only narrowing the gap discussed in section II. This can be seen from Table 2.

Such results are pessimistic for having neglected the fringing field. As a further guarantee that the chosen geometries of the lateral perforations do not have a great impact on the sensitivity, a numerical simulation has been carried out with COMSOL Multiphysics® though which the neglected fringing field is properly considered. The resulting capacitances per unit length of all configurations are higher than those calculated neglecting the fringing field, as shown in Table 3.

Table 2
Air specific capacitance C_c/L and sensitivity S of sensor probes with continuous contour removed from the plate surfaces (assuming $\varepsilon_{r,liq} = 2.15$) and their reduction relative to the probe with no slit and same geometrical parameters.

slit contour	C_c/L [pF/m]	S [pF/m]	drop [%]
no slit	722	830	–
straight	709	815	1.8
helix	668	768	7.53

6. Structural robustness to vibrations

6.1. Source of vibrations on helicopters

In special operating conditions, e.g., characterized by significant vibrational stresses, the behavior of the sensor might be undermined, should the plates be set in relative motion or even get in touch with each other. These conditions can introduce noise in the measurement due to capacitance value fluctuation and short circuit which would result, respectively.

This is only one of the problems affecting any kind of measurements made with in-flight sensors and it was addressed in many ways such as proposed in [26]. Another study was conducted in [27], even though drones are considered there, but the same applies to aircrafts.

Helicopter flight is one such special operating condition which is now examined to determine the highest possible value of the fundamental frequency of vibrational stresses that are transmitted to an on-board sensor.

The problem of vibrations of helicopters are much more pronounced than those on conventional aircrafts, where the turbo-propeller or the jet engine operate in axial flow and set up no noticeable variable stresses on structural elements and equipment during normal flight conditions. On the other hand, helicopter blades operate in an asymmetric velocity flow because they rotate in a plane that is almost transversal to the direction of motion. For this reason, they are subjected to variable aerodynamic loads in consequence of the periodically changing relative flow velocity during each turn while the helicopter advances.

These aerodynamic forces and moments acting on the blades are transmitted through the hub hinges to the rotor hub (Fig. 6a) and then to the fuselage and to all the equipment it hosts.

Vibration frequency can be determined the following simple reasoning [28]: during any steady state operating condition, with the helicopter holding on a given attitude, the rotor uniformly turns at constant angular speed ω, and the airflow velocity $\vec{V}$ is constant. At a given instant of time the blades are subjected to a certain aerodynamic stress depending on their angular positions, and consequently they transmit a certain system of forces and moments to the rotor hub (Fig. 6b).

This system is going to change with time because angular positions of blades change and with them also the airflow pattern will change. Once the blades reposition themselves in the next arrangement geometrically equivalent to that just considered, that is, after an angle equal to $2\pi/n$, where n is the number of blades, the airflow must take on the same pattern it had. It follows that the frequency of the vibrations transmitted to the fuselage through the rotor hub is equal to the rotor speed in turns per second times the number of blades, even though the stresses on each single blade are periodic in time with a period equal to the rotor speed. That means that harmonic components of the stresses of each blade cancel each other out if their frequency is not an integer multiple of the number of blades times the rotor speed, as is proved in [28]. Control strategies to counterbalance such fatigue stresses on the blades are an area of active research [29].

Typical values of rotor speeds are of at most 500 rpm for small

Table 3
Comparison between air specific capacitances C_c/L calculated without taking into consideration the fringing field with formulae (3), (18) and (20) and those simulated with COMSOL Multiphysics®, for all three probe configurations.

slit contour	C_c/L [pF/m] (fringing field is neglected)	C_c/L [pF/m] (fringing field is considered)
no slit	722	725
straight	709	723
helix	668	718

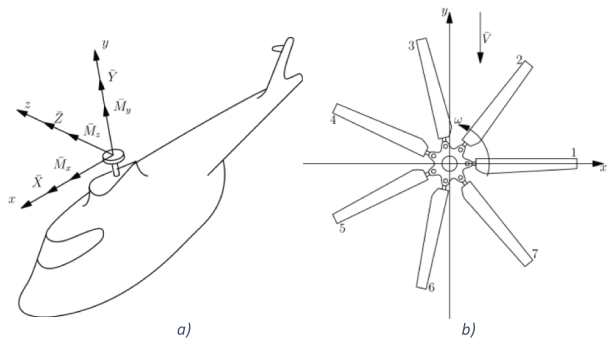

Fig. 6. a) Components of total forces and moments of blade set acting on the helicopter through the rotor hub. B) 7-blade propeller turning at uniform angular speed ω in a constant velocity $\vec{V}$ airflow field.

helicopters with 2 blades to approximately 225 rpm for big helicopters which can have as many as 7 blades. It is evident that higher values of vibration frequencies are those occurring in helicopters with many blades and then the typical highest value is about 26 Hz.

6.2. Flexural modes of the conventional-design sensor

In the following, only flexural vibrations are considered because longitudinal and torsional ones do not alter the relative position of the plates. Each plate can be seen as a beam that is clamped at an end where it is fixed to the tank roof and free at the other. Applying the dynamic equilibrium with these boundary conditions using the Euler-Bernoulli beam model, the natural frequencies of the flexural modes of vibration are given by [30]:

$$f_n = \frac{1}{2\pi L^2}\sqrt{\frac{EJ}{\rho A}}(\gamma_n L)^2 \tag{21}$$

where $n = 1, 2, 3, \cdots$ is the mode index, L is the length of the plate, E the Young's modulus of plate material, ρ its density, A is the cross-section area of the plate, and the γ_n's are the solutions of the following transcendental equation in the unknown γ:

$$cos(\gamma L)cosh(\gamma L) = -1 \tag{22}$$

which comes from the boundary value problem. The first three modes are provided in the following table.

Fig. 7 shows the corresponding modes of vibration obtained through finite element method (FEM) which, as an aside, confirmed natural frequency values from the Euler-Bernoulli model.

Among the plates, the internal one has the lowest natural frequency (69 Hz) which is greater than the 26 Hz of the fundamental harmonic component of the vibrations, thereby guaranteeing the structural robustness of the conventional-design sensor.

6.3. Flexural modes of the narrowed-gap sensors with straight and helical slits

The continuous end-to-end lengthwise perforation of the plates causes a drastic reduction of their natural resonant frequencies, so much that the fundamental frequency of the vibrational stresses exceeds the frequency of the first mode of vibration of the plate. Hence, to mitigate this drop, the perforation is made along a contour with solutions of continuity. Moreover, that contour stops at 33.5 mm from the end borders of the cylinder, so the surface regions in proximity of both ends are left intact.

For the straight contour case, just one solution of continuity is adopted and it is placed at the middle of the plate and extends for 67 mm (Fig. 8).

From the structural viewpoint, the problem is no more cylindrically symmetrical. Orienting the plate in an orthogonal coordinate system such that its longitudinal axis coincides with the Z axis and the perforation lies in the XZ plane, different orthogonal modes of vibration in the XZ and YZ planes result, as depicted in Fig. 9 with the help of a FEM-based computation. Correspondingly, the frequencies of the mode with same order number are slightly different as shown in the Table 4.

The limiting natural frequency of 67 Hz, relevant to the first mode in the YZ plane of the internal plate, is almost the same as that of the conventional-design sensor, namely 69 Hz. Then it can be concluded that the sensor with the proposed discontinuous straight-slit plates is as robust to vibrations as the conventional design one.

For the helical contour case, multiple interruptions (69 in total, 7.5 mm long each) of the contour are needed to limit the drop of the natural frequencies. They are regularly distributed in such a way that no privileged radial direction arises, as illustrated in Fig. 10.

No heterogeneity results among radial planes contrary to the previous case, thereby modes of vibration and their frequencies with same order number are the same in both XZ and YZ planes. Obtained through FEM computation they are shown in Table 5 and Fig. 11.

Again, the critical plate is the internal one whose first mode of flexural vibration has a frequency of 37 Hz, less than that of the previous cases but still greater than the upper end of the off-limit frequency range of 26 Hz. This assures the structural robustness of this design also in presence of in-flight helicopter vibrations (see Table 6.).

7. Conclusions

In this paper, building upon the conventional design of typical capacitive level sensors (CLS) employing a cylindrical capacitor, three suitable design variations were set out. The aim of this work was to tackle the known CLS inconveniences, i.e., poor static and dynamic characteristics, and at the same time confirm its highly appreciated benefits of robustness, reliability, continuous reading, unneeded maintenance.

A first design variation of the CLS, consisting in narrowing the gap

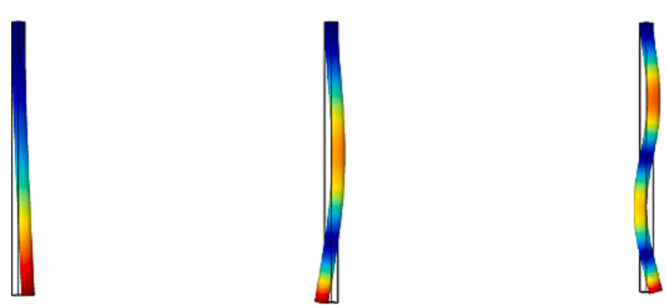

Fig. 7. First three flexural modes of vibration of a cylinder tube.

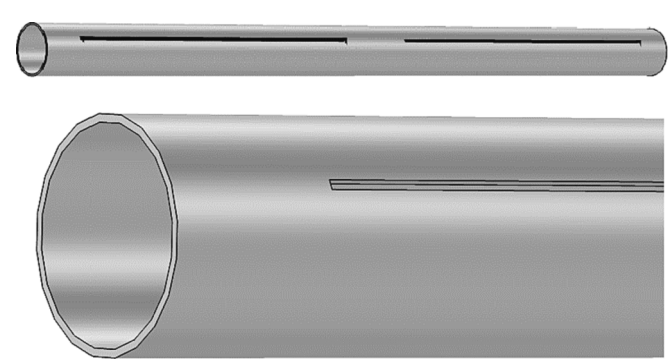

Fig. 8. Cylinder plate with a lengthwise straight slit interrupted halfway.

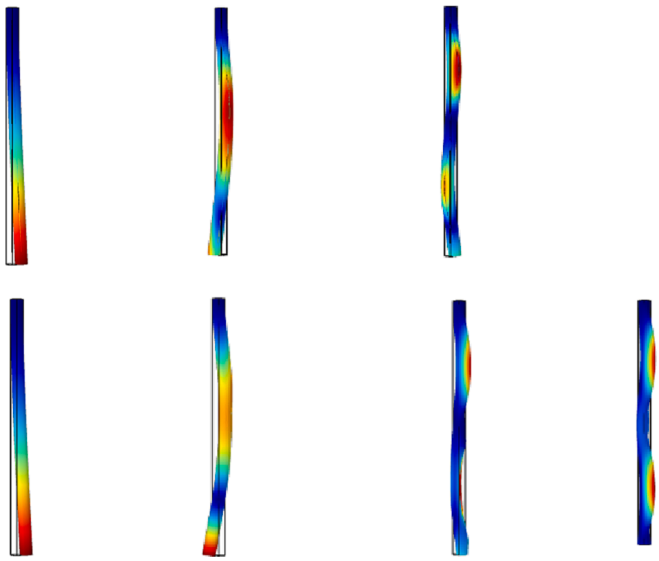

Fig. 9. First 3 flexural modes of vibration in YZ plane and first 4 in XZ plane of a cylinder tube with 2 lengthwise slits in the XZ plane.

Table 4
Frequencies of the first three flexural modes of vibration of the cylindrical plates. These values coincide with those obtained through FEM simulation.

	Internal plate [Hz]	External plate [Hz]
f_1	69	86
f_2	430	540
f_3	1200	1500

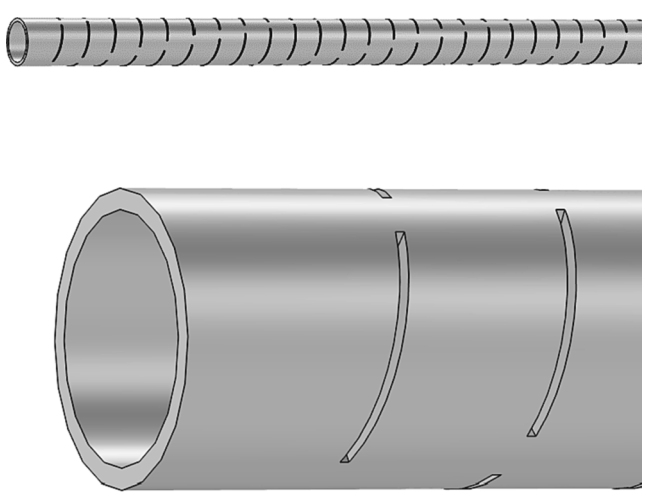

Fig. 10. Cylinder plate with a discontinuous lengthwise helical slit.

Table 5
Flexural vibration natural frequencies of a cylinder plate with two lengthwise straight slits in XZ plane.

	Internal plate [Hz]	External plate [Hz]
f_{1YZ}	67	83
f_{1XZ}	70	87
f_{2YZ}	296	361
f_{2XZ}	423	516
f_{3XZ}	682	741
f_{4XZ}	747	823
f_{3YZ}	944	1170

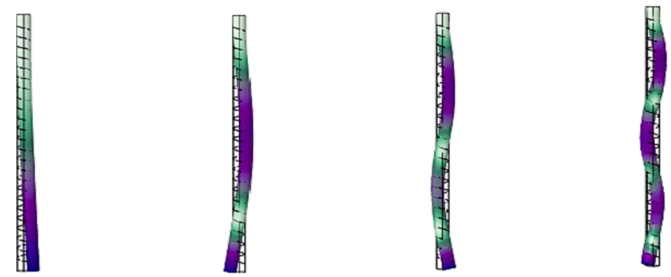

Fig. 11. First 4 flexural modes of vibration of a cylinder tube with discontinuous helical slit.

Table 6
Frequencies of the first 4 flexural modes of vibration of the cylindrical plates with discontinuous helical slit.

	Internal plate [Hz]	External plate [Hz]
f_1	37	44
f_2	228	264
f_3	596	680
f_4	1050	1190

between the plates, is conceived recognizing that it improves sensor sensitivity with the help of an electrostatic analysis (section II). Unfortunately, with such a choice also capillary effect comes in, as was found through hydrostatic analysis in section III. However, at the same time, the dynamic response to liquid level changes improves. In fact, overshoot disappears and, even though only within the first 200 mm, settling time reduces to at most 1 s for step level changes of 5% FS, as is shown through the hydrodynamic analysis proposed in section IV.

A second design variation to eliminate capillarity and enhance responsiveness is thus envisaged which consists in perforating the lateral surface of the plates along a lengthwise contour. However, that entails two concerns: *i)* sensitivity reduction whose effect is nonetheless negligeable as is proved in section V still through an electrostatic analysis, and *ii)* lowering of critical vibrational frequencies. The latter is made harmless even on helicopters where vibrational stresses are significant, by adopting a third design variation consisting in introducing continuity solutions to the removed contour. This is demonstrated in section VI through a structural dynamics analysis.

As regards the two kinds of slits on the lateral surface of the plates, the helical one should have the merit of improving the response to liquid level changes with respect to the straight configuration. Indeed, the helical slits, which act as gates made to let the liquid in and out of the annular channel during level changes, are completely distributed around the border of the cross section at every height. This allows a more rapid flooding or depletion process than with the straight slit case. In the straight slit case, the channel flooding or depletion experiences a viscous delay that is more marked the farther from the slit, reaching a maximum at the channel zone diametrically opposed to the slit.

In Table 7 a qualitative comparison between the proposed CLS design, the conventional CLS design and the optical one described in [7] is proposed.

As can be seen, the proposed CLS is superior to the optical one in many aspects; the most important ones are the improved linearity and sensitivity, the simplicity of the reading electronic with associated high reliability and low cost. One negative aspect of the proposed CLS with respect to the others is the manufacturing cost, with special reference to the helically slitted one. This cost is high when considering the single prototype but can be reduced with large scale production.

With respect to the conventional CLSs, the achievements of the proposed discontinuous-slit and narrowed-gap design sum up to give *i)* an improved sensitivity that, for engine oils, increases to more than 700pF/m, *ii)* a lower cost even though surface perforation workmanship

Table 7
Qualitative comparison between the proposed CLS design, the conventional CLS design and the optical one proposed in [7].

	Proposed CLS (helical slits)	*Conventional CLS (simple holes)*	*Optical fiber*
Cost	Medium	Low	Very high
Readout cost/reliability	Low/High	Low/High	Very high/Very low
Manufacturing process	Complex	Simple	Simple (sensing winding)
Sensitivity	Very High	High	Not quantified
Linearity	High	Low	Very low
Settling time	Low	High	Very low
Temperature drift	1.5% FSR	1.5% FSR	High
EMI	Resistant if shielded	Resistant if shielded	High
Errors and hysteresis due to retention	Modeled	None	Uncertain

must be accounted for, *iii)* cancellation of systematic errors due to capillary phenomena and *iv)* dynamic response no longer characterized by a sluggish and swinging behavior.

The comparison with the optical sensor proposed in [7] also shows an improvement in the linearity and in the uncertainty due to the fluid held on the sensing part. It should also be noted that the lubricating oil is rather viscous and adheres to the surface of the fiber, which may result in large errors and hysteresis due to retention.

Moreover, when considering the probe and the reading electronics, the capacitive sensor setup proved to be more cost-effective than other technologies. The probe has the highest cost indeed: the price of manufacturing the only helicoidal electrodes in a single prototype was about 1,500 USD, whilst the reading electronics is in the order of only 50 USD for a single prototype. Of course, these costs will be scaled down with mass-production. On the other hand, costs for optical sensors are way higher, in the order of the tens of thousands USD, about one order difference. This is mainly due to the cost of the light emitter and detector.

Extensive experimental verification of the theoretical results here obtained are being carried out considering additional sources of uncertainty: oil contamination, presence of metallic debris, temperature changes, parasitic capacitances, etc. First prototypes show the expected sensitivity, high linearity, and dynamical response in accordance with the simulations. From these verifications we also found that border effects due to the added slits are not observable. All the results of these investigations are going to be shared in a forthcoming paper.

Lastly, it would be convenient to integrate a level sensor with a quality sensor in a single sensing element: as an example, a cost-effective concentration sensor for liquid mixtures based on a dielectric resonator [31] or reflectometry [32,33] can be used as quality sensor. This work is also currently underway.

CRediT authorship contribution statement

Francesco Adamo: Investigation, Methodology, Resources, Supervision, Writing - review & editing. **Filippo Attivissimo:** Investigation, Methodology, Resources, Supervision, Funding acquisition, Project administration, Writing - review & editing. **Sergio de Gioia:** Investigation, Methodology, Resources, Formal analysis, Writing - original draft. **Daniel Lotano:** Investigation, Methodology, Resources, Supervision, Writing - original draft, Writing - review & editing. **Attilio Di Nisio:** Investigation, Methodology, Resources, Formal analysis, Supervision, Writing - review & editing.

Declaration of Competing Interest

The authors declare that they have no known competing financial interests or personal relationships that could have appeared to influence the work reported in this paper.

Data availability

Data will be made available on request.

Acknowledgments

This study has been developed in close cooperation with an international aerospace company within the Project “Future Revolutionary Technologies for Hybrid Electric Aircrafts”, funded by the Italian Ministry of University and Research through the research program PON R&I 2014-2020.

Appendix

Analytical derivation of (20) is here detailed. Moreover, a more compact form of (18) and (20) are given.

From (16) and (17), and putting

$$x(r) = \frac{2\pi r}{p} \tag{23}$$

(14) becomes

$$\frac{C_c}{L} = \frac{2\pi\varepsilon_0}{\int_{x_i}^{x_e} \frac{dx}{x\left(1-n_w\sqrt{1+x^2}\right)}} \tag{24}$$

where $x_e = x(r_e)$ and $x_i = x(R_i)$.

Then the integral at the denominator of (24), by variable substitution

$$x = \sinh\xi \tag{25}$$

becomes

$$\int_{sinh^{-1}x_i}^{sinh^{-1}x_e} \frac{cosh\xi d\xi}{sinh\xi(1 - n_w cosh\xi)} \tag{26}$$

and then, with trivial manipulation

$$-\frac{1}{n_w}\int_{sinh^{-1}x_i}^{sinh^{-1}x_e}\frac{[(1-n_w cosh\xi)-1]d\xi}{sinh\xi(1-n_w cosh\xi)} \tag{27}$$

which splits into

$$\left[-\frac{1}{n_w}\int\frac{d\xi}{sinh\xi}+\frac{1}{n_w}\int\frac{d\xi}{sinh\xi(1-n_w cosh\xi)}\right]_{sinh^{-1}x_i}^{sinh^{-1}x_e}. \tag{28}$$

The first integral evaluates to

$$\left[\ln\left|\frac{1-\cosh\xi}{\sinh\xi}\right|\right]_{\sinh^{-1}x_i}^{\sinh^{-1}x_e}=\ln\sqrt{\left|\frac{1-u}{1+u}\right|}\Bigg|_{u_i}^{u_e} \tag{29}$$

where the last step comes from applying the substitutions (25), (23), and (19).
The second integral, after a variable substitution,

$$u=\cosh\xi \tag{30}$$

that is the same as (19), transforms into

$$\int_{u_i}^{u_e}\frac{du}{(u^2-1)(1-n_w u)} \tag{31}$$

whose integrand breaks up, by partial fraction decomposition

$$\frac{1}{(u^2-1)(1-n_w u)}=\frac{A}{u-1}+\frac{B}{u+1}+\frac{C}{1-n_w u} \tag{32}$$

which gives

$$1=A(u+1)(1-n_w u)+B(u-1)(1-n_w u)+C\left(u^2-1\right) \tag{33}$$

that can be easily solved for A, B, and C when computed in three different values of u, as here shown for $u=1,\ -1$, and 0, respectively

$$\begin{aligned}1&=2A(1-n_w)\\1&=-2B(1+n_w)\\1&=A-B-C\end{aligned} \tag{34}$$

providing

$$\begin{aligned}A&=\frac{1}{2(1-n_w)}\\B&=-\frac{1}{2(1+n_w)}\\C&=\frac{n_w^2}{1-n_w^2}.\end{aligned} \tag{35}$$

Then (31) can be easily integrated thus giving

$$\ln\left(\sqrt{\frac{|1-u|^{\frac{1}{1-n_w}}}{|1+u|^{\frac{1}{1+n_w}}}}\ \frac{1}{|1-n_w u|^{\frac{n_w}{1-n_w^2}}}\right)\Bigg|_{u_i}^{u_e} \tag{36}$$

which put together with (29) back in (28) gives

$$\ln\left(\frac{\sqrt{|1-u|^{\frac{1}{1-n_w}}|1+u|^{\frac{1}{1+n_w}}}}{|1-n_w u|^{\frac{1}{1-n_w^2}}}\right)\Bigg|_{u_i}^{u_e} \tag{37}$$

that, noting that $\sqrt{|1-u||1+u|}=x$, can be rewritten as

$$\ln\left(x\sqrt{\frac{|1-u|^{\frac{n_w}{1-n_w}}}{|1+u|^{\frac{n_w}{1+n_w}}}}\ \frac{1}{|1-n_w u|^{\frac{1}{1-n_w^2}}}\right)\Bigg|_{u_i}^{u_e} \tag{38}$$

which is exactly the denominator of (20).
The limit of C_h/L considered as function of p by virtue of (19) is clearly

$$\lim_{p\to\infty}\frac{C_h(p)}{L}=\frac{2\pi\epsilon_0}{\ln\left[\frac{r_e}{R_i}\sqrt{\left|\lim_{p\to\infty}\frac{1-u_e(p)}{1-u_i(p)}\right|^{\frac{n_w}{1-n_w}}}\right]} \tag{39}$$

where the limit in the right-hand side after a convenient change of variable $p\to 1/p$ and applying de l'Hospital twice equals

$$\lim_{1/p\to 0}\frac{[1-u_e(1/p)]''}{[1-u_i(1/p)]''}=\left(\frac{r_e}{R_i}\right)^2 \tag{40}$$

which put back in (39) gives (18).

References

[1] B.S.N. Chandra, J. Roopa, A. Harigovind, A. Bharadwaj, A Review on Capacitive Liquid Level Sensing Techniques, J. Univ. Shanghai Sci. Technol. 23 (6) (2021) 654–662.

[2] C.S.S. Babu, P. Manohari, Studies on Effect of Corrosion for the Selection of Material of Self-Compensated Capacitive Type Liquid Level Sensor, Appl. Mech. Mater. 895 (2019) 230–236.

[3] R.T. Bento, R.W.O. Silva, L.A. Dias, A.F. Filho, A.J.C. Pitta, Design, development and application of a real-time capacitive sensor for automatically measuring liquid level, SN Appl. Sci. 1 (2019) 734, https://doi.org/10.1007/s42452-019-0770-3.

[4] L. Yin, Y. Qin, X.-W. Liu, A new interface weak-capacitance detection ASIC of capacitive liquid level sensor in the rocket, Mod. Phys. Lett. B 31 (32) (2017) 1750302, https://doi.org/10.1142/S021798491750302X.

[5] C.-S.A. Gong, H.K. Chiu, L.R. Huang, C.H. Lin, Z.D. Hsu, P.-H. Tu, Low-Cost Comb-Electrode Capacitive Sensing Device for Liquid-Level Measurement, IEEE Sensors Journal 16 (9) (May 1 2016) 2896–2897, https://doi.org/10.1109/JSEN.2016.2524696.

[6] B. Jin, Z. Zhang, H. Zhang, Structure design and performance analysis of a coaxial cylindrical capacitive sensor for liquid-level measurement, Sens. Actuators, A 223 (2015) 84–90, https://doi.org/10.1016/j.sna.2014.12.027.

[7] C. Zhao, L. Ye, J. Ge, J. Zou, X. Yu, Novel light-leaking optical fiber liquid-level sensor for aircraft fuel gauging, Opt. Eng. 52 (1) (4 January 2013), 014402, https://doi.org/10.1117/1.OE.52.1.014402.

[8] G. Andria, F. Attivissimo, A. Di Nisio, A. Trotta, S.M. Camporeale, P. Pappalardi, Design of a Microwave Sensor for Measurement of Water in Fuel Contamination, Measurement 136 (2019) 74–81.

[9] G.L. Tan, C.L. Zhu, P. Shen, W.P. Sun, C. Wu, Aircraft Fuel Volume Characteristic Calculations and Multi-Sensor Technology on Fuel Volume Measurement Simulation, Appl. Mech. Mater. Trans. Tech Publications Ltd (October 2015), https://doi.org/10.4028/www.scientific.net/amm.799-800.927.

[10] A.A. Kazemi1, C. Yang, S. Chen. "Fiber Optic Liquid-Level Sensor System for Aerospace Applications". In Micro- and Nanophotonic Technologies (eds P. Meyrueis, M. Van de Voorde and K. Sakoda), 2017. https://doi.org/10.1002/9783527699940.ch20.

[11] G. Onorato, G. Persichetti, I.A. Grimaldi, G. Testa, R. Bernini, Optical fiber fuel level sensor for aeronautical applications, Sens. Actuators, A 260 (2017) 1–9, https://doi.org/10.1016/j.sna.2017.04.015.

[12] F. Adamo, F. Attivissimo, S. de Gioia, A. Di Nisio, D. Lotano, M. Savino, Development and Prototyping of a Capacitive Oil Level Sensor for Aeronautical Applications. 25th IMEKO TC4 International Symposium, Sept 2022 to be published.

[13] De Palma, L., F. Adamo, F. Attivissimo, S. de Gioia, A. Di Nisio, A. Lanzolla, and M. Scarpetta, "Low-cost capacitive sensor for oil-level monitoring in aircraft", Instrumentation and Measurement in Aerospace and Space Systems of 2022 IEEE International Instrumentation and Measurement Technology Conference (I2MTC), Ottawa, Canada, May 16-19, 2022.

[14] J.R. Hanni, S.K. Venkata, A novel helical electrode type capacitance level sensor for liquid level measurement, Sens. Actuators, A 315 (2020), https://doi.org/10.1016/j.sna.2020.112283.

[15] Loconsole, A. M., V. V. Francione, V. Portosi, O. Losito, M. Catalano, A. Di Nisio, F. Attivissimo, and F. Prudenzano "Substrate-Integrated Waveguide Microwave Sensor for Water-in-Diesel Fuel Applications," Applied Sciences, vol. 11, novembre 2021, pp. 1-18.

[16] O.P. Sondhiya, Amit Kumar Gupta, "Wear debris analysis of automotive engine lubricating oil using by ferrography", Int. J. Eng. Innov. Technol. 2 (5) (2012) 46–54.

[17] G. Andria, F. Attivissimo, A. Di Nisio, A. Trotta, S.M. Camporeale, P. Pappalardi, Design of a Microwave Sensor for Measurement of Water in Fuel Contamination, Measurement 136 (March 2019) 74–81.

[18] European Standard EN 10220:2002 - Seamless and welded steel tubes - Dimensions and masses per unit length," European Committee for Standardization, Dec. 2002.

[19] H. Sun, Y. Liu, J. Tan, Research on Testing Method of Oil Characteristic Based on Quartz Tuning Fork Sensor, Appl. Sci. 11 (12) (2021) 5642, https://doi.org/10.3390/app11125642.

[20] J.G. Seebold, M.P. Hollister, H.M. Satterlee, Capillary hydrostatics in annular tanks, J. Spacecr. Rocket. 4 (1) (1967).

[21] R. De Luca, O. Faella, "Communicating vessels: a non-linear dynamical system", Revista Brasileira de Ensino de Física 39 (3) (2017) e3309.

[22] R.F. Lacouic, J. A. Berm, "Capillary Rise in the Annular Region of Concentric Cylinders During Coast Periods of Atlas-Centaur flights," Lewis Research Center, Cleveland, Ohio, NASA Techincal Memorandum X-1558 (May 1968).

[23] D.J. Griffiths. *Introduction to Electrodynamics* (4th ed.). Cambridge: Cambridge University Press (2017). doi:10.1017/9781108333511.

[24] V.L. Streeter, E.B. Wylie, K.W. Bedford, Fluid Mechanics, 9th ed., MA, USA, WCB McGraw-Hill, Boston, 1998.

[25] R.B. Bird, W.E. Stewart, E.N. Lightfoot, Transport Phenomena, (2nd ed.)., John Wiley & Sons Inc., New York, NY, USA, 2002.

[26] I.E. Davydov, E.I. Davydov, Liquid oscillations in the tanks' level sensors of aerospace objects, AIP Conf. Proc. 1798 (2017), 020044, https://doi.org/10.1063/1.4972636.

[27] P. Daponte, L. De Vito, F. Lamonaca, F. Picariello, S. Rapuano, M. Riccio, in: Measurement science and education in the drone times, 2017, pp. 1–6, https://doi.org/10.1109/I2MTC.2017.7969979.

[28] Mil', M. L., et al. (1967). *Helicopters – Calculation and design: Vol. II. Vibrations and Dynamic Stability*. Mashinostroyeniye Press: Moscow.

[29] A. Rossi, F. Orsini, A. Scorza, F. Botta, F. Leccese, E. Silva, K. Torokhtii, I. Bernabucci, S.A. Sciuto, A preliminary performance validation of a MEMS accelerometer for blade vibration monitoring, in: in Proceedings of the 22nd IMEKO TC4 International Symposium & 20th International Workshop on ADC Modelling and Testing Supporting World Development through Electrical & Electronic Measurements, September 2017, pp. 14–15.

[30] M. Avcar, Free Vibration Analysis of Beams Considering Different Geometric Characteristics and Boundary Conditions, Int. J. Mech. Appl. 4 (3) (2014) 94–100.

[31] Mayani, M. G., F. J. Herraiz-Martínez, J. M. Domingo, R. Giannetti and C. R. -M. García, "A Novel Dielectric Resonator-Based Passive Sensor for Drop-Volume Binary Mixtures Classification," in IEEE Sensors Journal, vol. 21, no. 18, pp. 20156-20164, 15 Sept.15, 2021, doi: 10.1109/JSEN.2021.3094904.

[32] M. Scarpetta, M. Spadavecchia, F. Adamo, M. A. Ragolia, and N. Giaquinto, "Detection and Characterization of Multiple Discontinuities in Cables with Time-Domain Reflectometry and Convolutional Neural Networks," Sensors, vol. 21, no. 23, pp. 8032–8032, Dec. 2021, doi: 10.3390/s21238032.

[33] M. Scarpetta, M. Spadavecchia, G. Andria, M.A. Ragolia, N. Giaquinto, Analysis of TDR Signals with Convolutional Neural Networks, in: in 2021 IEEE International Instrumentation and Measurement Technology Conference (I2MTC), May 2021, pp. 1–6, https://doi.org/10.1109/I2MTC50364.2021.9460009.